# Nanoscale

Accepted Manuscript


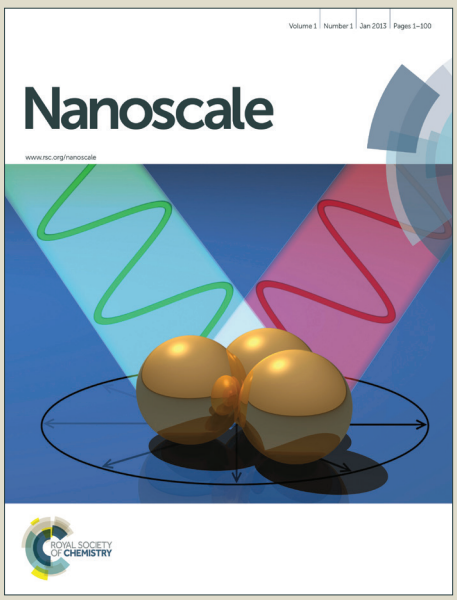





ROYAL SOCIETY OF CHEMISTRY

www.rsc.org/nanoscale

# Antisite Defects in Layered Multiferroic $CuCr_{0.9}In_{0.1}P_2S_6$

Qian He,[1,*] Alex Belianinov,[2] Andrius Dziaugys,[3] Petro Maksymovych,[2] Yulian Vysochanskii,[4] Sergei V. Kalinin[2] and Albina Y. Borisevich[1,2,*]

[1] Materials Science and Technology Division, Oak Ridge National Laboratory, Oak Ridge, Tennessee, 37831, United States.

[2] The Institute for Functional Imaging of Materials and the Center for Nanophase Materials Sciences, Oak Ridge National Laboratory, Oak Ridge, Tennessee, 37831, United States.

[3] Department of Radiophysics, Faculty of Physics, Vilnius University, 2600, Lithuania

[4] Institute of Solid State Physics and Chemistry, Uzhgorod University, Uzhgorod, Ukraine 88000

* Corresponding authors (Qian He: heqian.lehigh@gmail.com; Albina Borisevich: albinab@ornl.gov)

**Abstract**

$CuCr_{1-x}In_xP_2S_6$ system represents a large family of metal chalcogenophosphates that are unique and promising candidates for 2D materials with functionalities such as ferroelectricity. In this work, we carried out detailed microstructural and chemical characterization of these compounds using aberration-corrected STEM, in order to understand the origin of these different ordering phenomena. Quantitative STEM-HAADF imaging and analysis identified stacking order of an 8-layer thin flake, which leads to the identification of anti-site $In^{3+}(Cu^{+})$ doping. We believe these findings will pave the way towards understanding of the ferroic coupling phenomena in van der Waals lamellar compounds, as well as their potential applications in 2-D electronics.

The discovery of graphene has brought intense research focus onto novel 2D materials with additional functionalities,[1–5] such as insulating BN[6] and semiconducting metal dichalcogenides.[7] It is also very interesting to look for 2D materials with ferroelectric and ferromagnetic properties, which will enable bi- and multi-stable devices and functional electronics in 2D form. In addition, since ferroelectric oxide gated graphene was already shown to bring enhanced mobility,[8] memory effect[9,10] and optoelectronic properties,[11] heterostructures and interfaces between the possible 2D ferroic materials with graphene become promising. Last but not least, 2D ferroic materials have potential applications in ferroelectric and multiferroic based tunneling devices.[12]

One promising candidate for 2D ferroic material is the wide family of metal chalcogenophosphate $M^{I}M^{III}P_2X_6$ (where $M^{I}$ = Cu, Ag; $M^{III}$ = Cr, In, Bi, Mn and etc; X = S, Se ) crystals with different types of dipole and spin ordering.[13–15] Particular interest has been focused on $CuInP_2S_6$ related compounds, which have a van-der-Waals layered crystal structure and room temperature ferrielectric phase.[16,17] Isovalent cation doping can significantly modify the properties of this material. Substituting In with Cr will eventually result in a multiferroic compound $CuCrP_2S_6$ that has antiferroelectric and antiferromagnetic ordering below 150K and 32K respectively.[15,18] A more complicated picture is found in the intermediate composition $CuCr_{1-x}In_xP_2S_6$, as shown by the phase diagram in Figure 1(a).[19] A dipolar glass state exists in $0.2 < x < 0.7$ range. It even appears that the ferrielectricity and dipolar glass coexist at low temperatures for indium concentrations around $x = 1$. A multiglass state was also reported at low temperatures in for some concentrations ($0.2 < x < 0.3$), where the dipole glass possibly could coexist with the spin glass. Such multiglass phase has been studied for oxide perovskite solutions $Eu_xSr_{1-x}TiO_3$[20,21] and it is a promising functional material with a biquadratic interaction between electric and magnetic fields. The origin of these glass phases is of significant fundamental interest.

It is not yet clear how the dopant distribution may affect the spin/dipole ordering in the host material. $CuCrP_2S_6$ (Figure 1 (b)) and $CuInP_2S_6$ (Figure 1 (c)) both have monoclinic lattices with layers that have identical structure, in which Cu, In or Cr, and P-P pairs ($P_2$) form sparse honeycomb sub-lattices.[15,16] However the stacking sequences of these layers in the two compounds are different. One way to express this difference is as follows: in order to position the second layer, it needs to rotate 180$^o$ with respect to the first layer and then shift $1/2\,\vec{c}^* + 1/3\,\vec{a}$ (or equivalently$1/2\,\vec{c}$), but the rotation center is Cu site for $CuCrP_2S_6$ and In site for $CuInP_2S_6$. Therefore the structure for $CuCr_{1-x}In_xP_2S_6$ with intermediate compositions cannot be easily extrapolated from the end members, and some structural frustration can result. Aberration-corrected scanning transmission electron microscopy (STEM)[22], which is capable of providing structural and chemical information at sub-Å spatial resolution, is an ideal tool to study dopant distribution in this material.[23,24]

As shown in (Figure 2 (a-c)), a roughly 10 μm long, 4 μm wide specimen was obtained via the "scotch tape" method (see supplemental information). Its thickness was measured by AFM to be about 5 nm, an equivalent of 8 layers (layer thickness is 0.64 nm for $CuCrP_2S_6$). Figure 2(d) shows a section of a HAADF image of this flake viewed from [102] zone axis (full image is shown in Figure S1), while in some other regions the [001]* zone was observed (Figure S2) due to bending of the thin specimen. In these images, Cu, Cr and P sub-lattices can be observed, whereas the contribution of S framework is largely smeared into the background, as can be seen from the simulated image shown in Figure 2(e-g). Due to the Z-contrast nature of the HAADF imaging, the presence of In dopants (Z=49) is manifested as bright columns. In addition, since the Cu, Cr and P sub-lattices repeat itself every 4 layers in the [102] zone projection, the image can be split into four two-layer subsets. As the lateral shift/rotation of the layers is connected to their vertical position in a known pattern, these provide us an opportunity to investigate In dopant distribution not only in the image plane, but also in the third dimension.

Quantitative image intensity analysis was carried out to locate In dopants for the HAADF image shown in Figure S1. A total of 7308 atomic columns were included in this analysis. After locating the atomic columns using the center of mass approach, the background was first estimated by averaging the intensity at the middle point of the distance to each nearest neighbor column. Since this is done for each atomic column locally, the uneven background caused by hydrocarbon contamination can be removed (Figure S1). Then, the corrected column intensities were analyzed for each layer pair (i.e. #1/#5, #2/#6, #3/#7 and #4/#8) and for each honeycomb sub-lattices (red, blue and black). While it is not straightforward to designate those to Cu, Cr, and P sublattices immediately, the stacking relations enable us to identify the same sublattice within different layer pairs. The resultant intensity histograms are shown in Figure 3; note that P sublattice has double the occupancy of the Cu and Cr ones and thus all three have comparable intensities. There are two distinctive features in these intensity histograms: (i) in each layer pair there is always one sub-lattice (labeled blue) that has the lowest average intensity; (ii) The intensity distribution of each sub-lattice appears to follow a Gaussian curve, however only the blue and red columns have a distinctive secondary maximum at higher intensities, which indicates that the In dopants are present in both blue and red columns but not the black ones.

It is conventionally thought that $In^{3+}$ dopants should occupy the isovalent $Cr^{3+}$ sites to maintain local charge balance. Therefore, it is rather surprising to find that In dopants are occupying two types of columns. One possible explanation is that there may be stacking faults developed in the system, which are either intrinsic defects or extrinsic defects induced during mechanical exfoliation. For an 8-layer specimen, the number of possible stacking patterns is enormous. Fortunately, since the 8-layer can be decomposed into 4 pairs of double layers from the [102] projection, the number of possible arrangements reduces to 6. STEM Image simulations[25] were then carried out to investigate all 6 possible arrangements. Normalized column intensities for experimental data (mean value of the main Gaussian peaks in Figure 3), simulated results for normal stacking and one type of stacking fault arrangement

(with intensity distribution closest to experimental) are shown in Figure 4. From the experimental data, (A) red, (B) black and (C) blue columns have a relative mean intensity of 100%, 99% and 79% respectively, with 99.9% confidence interval of $\pm 1\%$ assuming Student t-distribution. These are in close agreement with the simulated intensity ratios for the case of normal stacking and, therefore, we rule out the possibility of stacking faults in this 8-layer specimen. The detailed simulation results and the histograms for all 6 types of stacking faults can be found in Figures S3 and S4. Using this information, we can then assign the column C (blue) in Figure 3 as Cr. With additional assumption that In is not going to substitute two P atoms to alter the $P_2S_6$ framework, A (red) and B (black) columns can also be assigned as Cu and P respectively. Thus we not only successfully decipher the stacking sequence of this 8-layer thin specimen, but also detect that In dopants can occupy both Cu (red) and Cr (blue) sites. An anti-site defect $In^{3+}(Cu^{+})$ was found.

We can further quantify how many anti-site defects $In^{3+}(Cu^{+})$ are there compared to the normal isovalent $In^{3+}(Cr^{3+})$ substitutions. Figure 5 shows the combined histograms of Cu, Cr and P2 sites, which are much less noisy as each histogram now has the intensities for 2436 atomic columns. The proportion of the sites that have In dopants can be estimated by the area underneath the fitted Gaussians. We can calculate the dopant concentration using the binomial model $Probability(n, p, k) = C_n^k p^k (1-p)^{n-k}$, where n=2 is the number of possible sites for each column, p is the dopant concentration, and k is the number of dopants in that column. As shown in Table 1, the results suggest that about the dopant concentrations are 4% for the isovalent $In^{3+}(Cr^{3+})$ doping and 6% for the anti-site $In^{3+}(Cu^{+})$ doping. The total 10% dopant concentration is consistent with the nominal composition of the compound. Clearly the anti-site $In^{3+}(Cu^{+})$ doping appears to be more favorable.

This discovery of the anti-site In doping will significantly change our current understanding of the phase diagram in the $CuCr_{1-x}In_xP_2S_6$ system. A more complete picture of the types of chemical disorder present in the system is needed in order to understand the observed order/disorder

transitions in spin and dipole systems in this material. The nonmagnetic In dopants were previously thought to decrease the exchange interactions of Cr cations and thus decrease the Neel temperature of the material. Now with the possibility of replacing of Cu cations, In dopants must also have significant influence of the interaction of dipoles, which mainly originate from the Cu sublattice.[18,19] We believe this finding will enable more realistic modeling of this material and accelerate progress towards understanding the ferroic coupling phenomena in van der Waals lamellar compounds. While the evidence for $In^{3+}(Cu^{+})$ antisite defects is clear, we have no reason to suggest that overall composition deviates from nominal. Indeed, two findings point in the opposite direction: i) the overall HAADF quantification matches very well with the ideal structure and ii) the overall dopant concentration acquired from statistical analysis matches well with the nominal value. It is, however, so far unclear how the *local* disruption of the charge balance created by the anti-site defects $In^{3+}(Cu^{+})$ is accommodated. Multiple options exist, including at least compensating $Cu^{+}(Cr^{3+})$ antisite defects, surface adsorbates[26] (can make a significant contribution for a thin flake) and mixed valances[27] of the $P_2S_6$ network. The exact compensation mechanism merits detailed investigation in the future.

## References


1 E. Morales-Narváez and A. Merkoçi, *Adv. Mater.*, 2012, **24**, 3298–308.

2 R. Ma and T. Sasaki, *Adv. Mater.*, 2010, **22**, 5082–104.

3 Y. Huang, J. Liang and Y. Chen, *Small*, 2012, **8**, 1805–34.

4 M. Osada and T. Sasaki, *Adv. Mater.*, 2012, **24**, 210–28.

5 R. Mas-Ballesté, C. Gómez-Navarro, J. Gómez-Herrero and F. Zamora, *Nanoscale*, 2011, **3**, 20–30.

6 D. Pacilé, J. C. Meyer, C. O. Girit and A. Zettl, *Appl. Phys. Lett.*, 2008, **92**, 133107.

7 M. Chhowalla, H. S. Shin, G. Eda, L.-J. Li, K. P. Loh and H. Zhang, *Nat. Chem.*, 2013, **5**, 263–75.

8 X. Hong, A. Posadas, K. Zou, C. Ahn and J. Zhu, *Phys. Rev. Lett.*, 2009, **102**, 136808.

9 Y. Zheng, G.-X. Ni, S. Bae, C.-X. Cong, O. Kahya, C.-T. Toh, H. R. Kim, D. Im, T. Yu, J. H. Ahn, B. H. Hong and B. Özyilmaz, *EPL (Europhysics Lett.*, 2011, **93**, 17002.

10 H. J. Hwang, J. H. Yang, Y. G. Lee, C. Cho, C. G. Kang, S. C. Kang, W. Park and B. H. Lee, *Nanotechnology*, 2013, **24**, 175202.

11 D. Jin, A. Kumar, K. Hung Fung, J. Xu and N. X. Fang, *Appl. Phys. Lett.*, 2013, **102**, 201118.

12 Z. Wen, C. Li, D. Wu, A. Li and N. Ming, *Nat. Mater.*, 2013, **12**, 617–21.

13 V. Maisonneuve, J. M. Reau, M. Dong, V. B. Cajipe, C. Payen and J. Ravez, *Ferroelectrics*, 1997, **196**, 257–260.

14 V. Maisonneuve, V. B. V. Cajipe, A. Simon, R. Von Der Muhll and J. Ravez, *Phys. Rev. B*, 1997, **56**, 860–868.

15 V. Maisonneuve, C. Payen and V. Cajipe, *J. Solid State Chem.*, 1995, **116**, 208–210.

16 V. Maisonneuve, M. Evain, C. Payen, V. B. Cajipe and P. Molinié, *J. Alloys Compd.*, 1995, **218**, 157–164.

17 A. Belianinov, Q. He, A. Dziaugys, P. Maksymovych, E. Eliseev, A. Borisevich, A. Morozovska, J. Banys, Y. Vysochanskii and S. V Kalinin, *Nano Lett.*, 2015, **15**, 3808–14.

18 W. Kleemann, V. V. Shvartsman, P. Borisov, J. Banys and Y. M. Vysochanskii, *Phys. Rev. B*, 2011, **84**, 094411.

19 A. Dziaugys, V. V. Shvartsman, J. MacUtkevic, J. Banys, Y. Vysochanskii and W. Kleemann, *Phys. Rev. B - Condens. Matter Mater. Phys.*, 2012, **85**, 134105.

20 W. Kleemann, *Solid State Phenom.*, 2012, **189**, 41–56.

21 E. a. Eliseev, M. D. Glinchuk, V. V. Khist, C. W. Lee, C. S. Deo, R. K. Behera and A. N. Morozovska, *J. Appl. Phys.*, 2013, **113**.

22 S. J. Pennycook and N. P.D., *Scanning Transmission Electron Microscopy: Imaging and Analysis*, Springer US, 2011.

23 R. Ishikawa, A. R. Lupini, S. D. Findlay, T. Taniguchi and S. J. Pennycook, *Nano Lett.*, 2014, **14**, 1903–1908.

24 P. M. Voyles, D. A. Muller, J. L. Grazul, P. H. Citrin and H.-J. L. Gossmann, *Nature*, 2002, **416**, 826–9.

25 E. J. Kirkland, *Advanced Computing in Electron Microscopy*, Springer Science & Business Media, 2010.

26 H. Nan, Z. Wang, W. Wang, Z. Liang, Y. Lu, Q. Chen, D. He, P. Tan, F. Miao, X. Wang, J. Wang and Z. Ni, *ACS Nano*, 2014, **8**, 5738–45.

27 K. Ichimura, H. Nakano and M. Takashima, *Mol. Cryst. Liq. Cryst. Sci. Technol. Sect. A. Mol. Cryst. Liq. Cryst.*, 2000, 341, 111–117.

**Acknowledgements:**

Q. H. and A. Y. B. (STEM characterization) are supported by the U.S. Department of Energy, Office of Science, Basic Energy Sciences, Materials Sciences and Engineering Division. A. B., (AFM characterization) P. M., S.V. K. are supported by the Center for Nanophase Materials Sciences, which is sponsored at Oak Ridge National Laboratory by the Scientific User Facilities Division, Office of Basic Energy Sciences, US Department of Energy. A. D. and Y. V. grew and provided the samples studied. All authors participated in manuscript discussion.

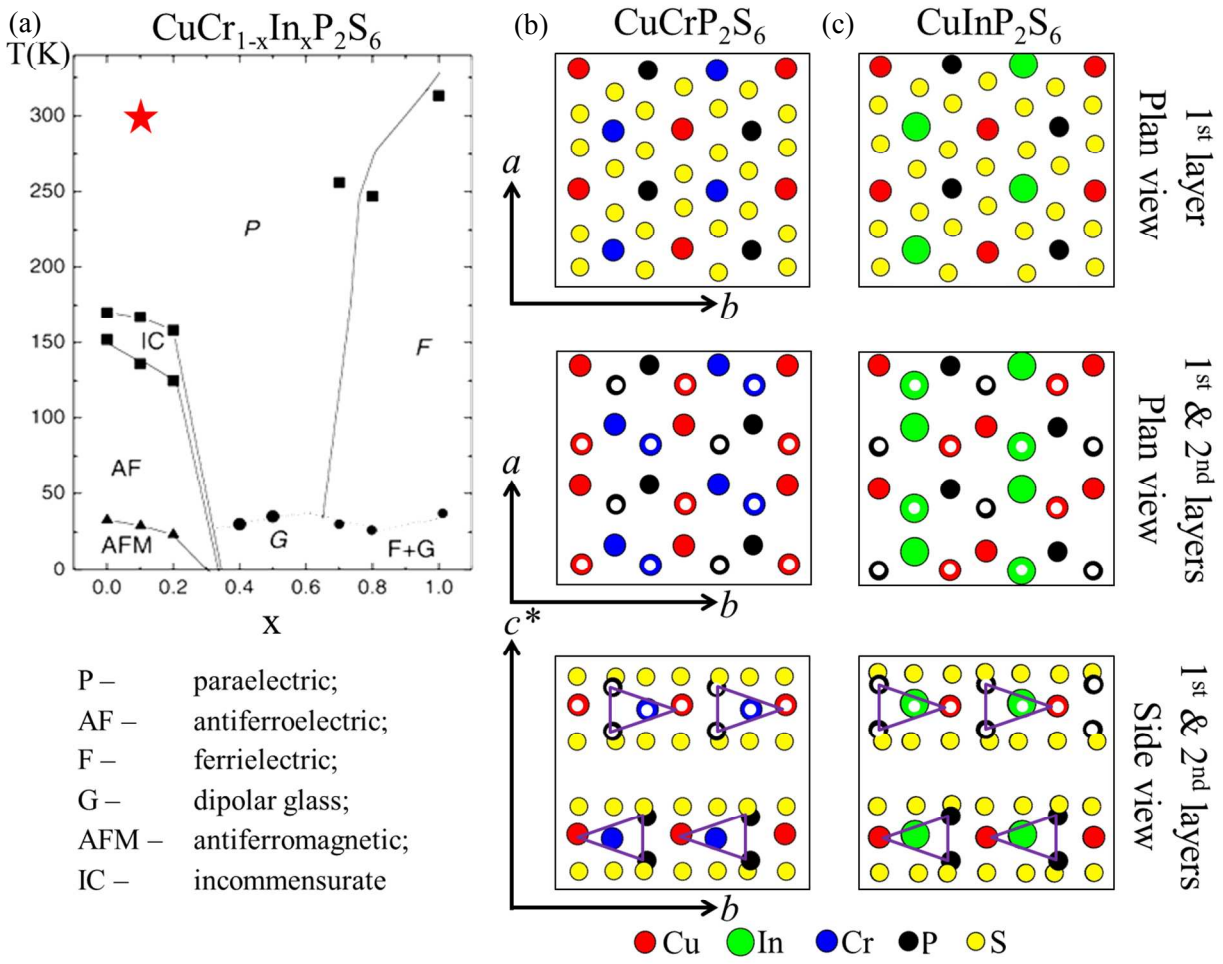


Figure 1 (a) Phase diagram of the $CuCr_{1-x}In_xP_2S_6$ system and the structural models for the two end members (b) $CuCrP_2S_6$ (x=0) and (c) $CuInP_2S_6$ (x=1). The top row shows the planar view of the individual layers (ab-plane). The second and third rows show the planar and side views of the stacking sequences. Sulfur atoms are not shown in the planar view for clarity. The 1st layer was labeled as solid circles while the 2nd layer was labeled as hollow circles. Different colors represent different atoms as: Cu – red, In – green, Cr – blue, P – black, S – yellow. The purple triangles in the bottom row models are drawn from P pairs towards Cu sites in order to highlight the stacking sequences. Basically, the second layer first rotates 180° and then shifts $1/2\,\vec{c}^{*} + 1/3\,\vec{a}$ (or $1/2\,\vec{c}$) compared to the first layer. The difference in the stacking for the two

compounds is that for $CuCrP_2S_6$, the rotation center is a Cu site, instead of an In site as in the case of $CuInP_2S_6$. As a result, the Cu columns are aligned in (020) planes in $CuCrP_2S_6$, while it is the In columns that are aligned in (020) planes for $CuInP_2S_6$. The red star in the phase diagram indicates the material that is studied in this paper.

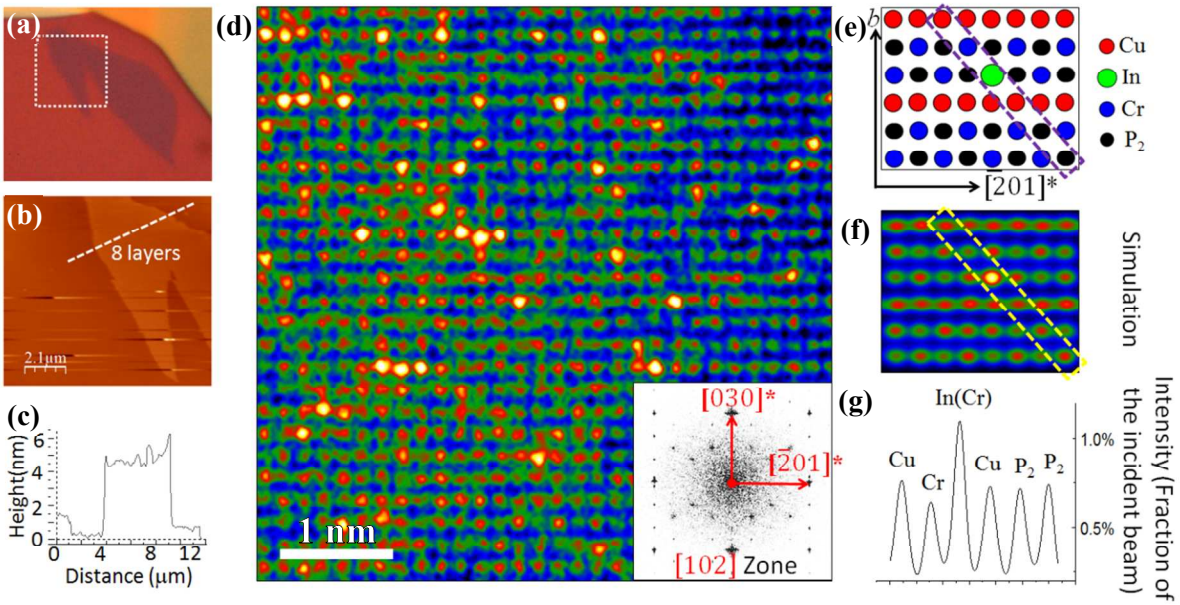


.

Figure 2 (a) Optical image of the exfoliated $CuCr_{0.9}In_{0.1}P_2S_6$ specimen (light purple area) on 300nm $SiO_2$/Si substrate; (b) AFM topography image of the specimen in the white dashed square in *(a)*. The height profile of the highlighted region is plotted in (c), which shows that the specimen has a thickness ~5 nm, corresponding to 8 layers. (d) STEM-HAADF image of the 8-layer $CuCr_{0.9}In_{0.1}P_2S_6$ specimen viewed from [102] zone. The inset in (d) shows the inverted diffractogram of the image. (e) Atomic model of the 8-layer $CuCrP_2S_6$ viewed from [102] zone, with one In dopant occupying one Cr site. (f) Multislice simulation using the model in (e) and the intensity line profile of the highlighted region is plotted in (g).

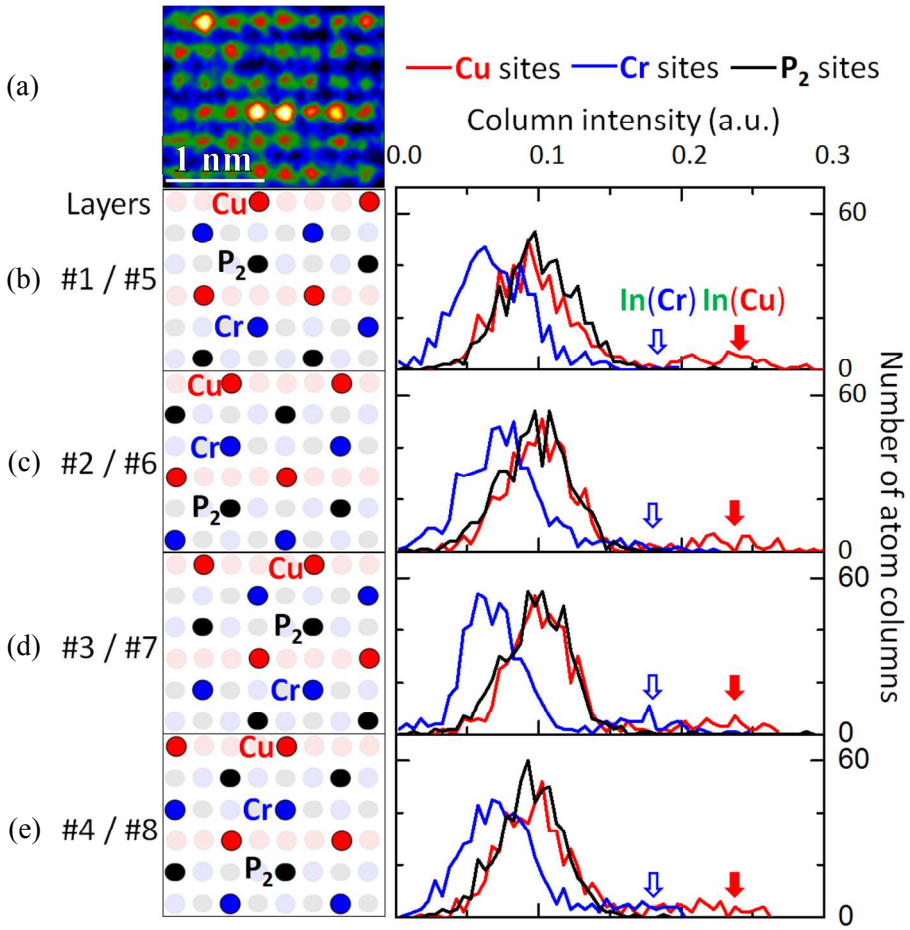


Figure 3 (a) A section of experimental STEM-HAADF image of the 8-layer $CuCr_{0.9}In_{0.1}P_2S_6$ specimen. (b-e) Column intensity statistics for each layer pairs. The highlighted atom sites in the model at the left are showing where the atom column intensity data is collected for each layer pair. In the ideal $CuCrP_2S_6$ structure, red, blue and black sites each contain distinct atoms. The intensity distribution for red, blue and black columns counted from one image with a large field of view ($87 \times 84 = 7308$ columns, see supplemental information). The red, blue and black columns can be assigned as Cu, Cr and $P_2$ columns respectively. The In dopants can be viewed from the intensity profile as higher intensity tails in each column. Surprisingly, both blue and red columns have such tail (highlighted in hollow blue and solid red arrows respectively),

suggesting the existence of anti-site doping of In on Cu sites (*i.e.* In(Cu)), in addition to the expected In(Cr).

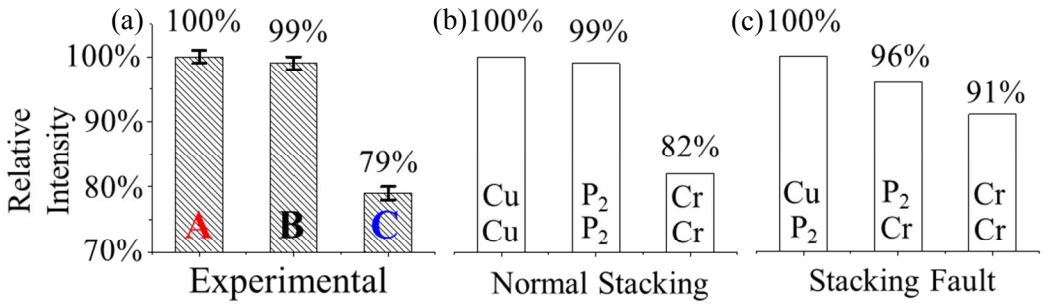


Figure 4 (a) Relative mean intensity of un-doped A sites (red), B sites (black) and C sites (blue) from Figure 3. The error bar shows $\pm 1\%$, which represent 99.9% confidence interval assuming student t-distribution. A similar analysis can be done on simulated images of $CuCrP_2S_6$ (b) without and (c) with one configuration of stacking faults. An exhaustive investigation of other configurations of stacking faults can be found in Figure S3 and S4. The experiment data matches best with the normal stacking. We can then assign the column C (blue) in Figure 3 as Cr. Cu and $P_2$ columns are assigned as A (red) and B (black) columns respectively, based on the assumption that In is not going to substitute two P atoms to alter the $P_2S_6$ framework.

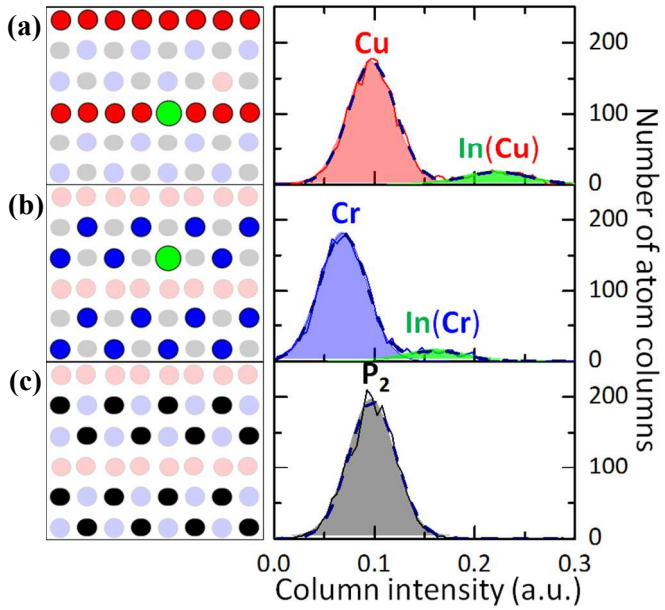


Figure 5 Gaussian statistics of the combined intensity profile for (a) Cu, (b) Cr and (c) $P_2$ columns in all 8 layers. The highlighted atom sites in the model shown at the left column are showing where the atom column intensity data is collected. The resultant intensity profiles are shown at the right column. The filled peaks are the Gaussian fitting of the intensity peaks. The presence of the second Gaussian peak (colored in green) in Cu (red) and Cr (blue) columns shows the presence of In doping. There are no In dopants found in $P_2$ (black) sublattice, which shows only one Gaussian peak in the intensity profile.

$$Probability\ (n, p, k) = C_n^k p^k (1-p)^{n-k}$$

| | | Gaussian Fitting Results | | | Binomial model | |
|---|---|---|---|---|---|---|
| # dopants | | **Cu sites** | **Cr sites** | **P sites** | n=2, p=6% | n=2, p=4% |
| | μ | 0.10 | 0.07 | 0.10 | – | – |
| k = 0 | σ | 0.02 | 0.02 | 0.02 | – | – |
| | A | ***88.3%*** | ***91.5%*** | – | *88.4%* | *92.2%* |
| | μ | 0.22 | 0.16 | – | – | – |
| k = 1 | σ | 0.03 | 0.03 | – | – | – |
| | A | ***11.7%*** | ***8.5%*** | – | *11.3%* | *7.7%* |

Table 1. Statistical results from Gaussian fitting in Figure 5 and the standard binomial distribution model for comparison. In the binomial mode, n is the number of trials (two cation sites for each column in an 8-layer specimen viewed from [102] zone), k is the number of successes (number of dopants) and p is the probability of success. μ is the mean and σ is the standard deviation in the Gaussian function. A is the area underneath the Gaussian peak, which is used to calculate the probability of k=0 (no dopants) and k=1 (one In dopant). The results of In(Cu) and In(Cr) agree well with the binomial distribution of p = 0.6 and p=0.4 respectively, indicating that ~60% of the In dopants are at Cu sites.